Energy 278 (2023) 127913

Contents lists available at ScienceDirect

Energy

journal homepage: www.elsevier.com/locate/energy

Evolution of pore structure and adsorption-desorption in oil shale formation rocks after compression

Xianfu Huang [a,b], Ya-Pu Zhao [a,b,*]

[a] State Key Laboratory of Nonlinear Mechanics, Institute of Mechanics, Chinese Academy of Sciences, Beijing, 100190, China
[b] School of Engineering Science, University of Chinese Academy of Sciences, Beijing, 100049, China

ARTICLE INFO

Handling Editor: Wojciech Stanek

Keywords:
Shale oil and shale gas
Adsorption-desorption ishotherms
BET specific surface area
Total pore volume
Fractal dimension
Carbon sequestration

ABSTRACT

As the extensive application of reservoir stimulation technologies such as hydraulic fracturing (including CO_2 fracturing) and in-situ conversion, identifying the developing rules of the pore structure in shale formations rocks after compression becomes all the more important. Here we carry out experimental studies to reveal the evolution mechanism of pore structure of oil shale formation rocks after compression primarily via adsorption-desorption isotherms. The results show that the BET specific surface area of the oil shale rocks first increases and then decreases after the confined compression, while the second dominant peak of pore size distribution shows the opposite behaviors. The pore volume experiences the stage of decrease, increase and continuous decrease with the increasing applied stress, and at last decreases by ~30% under 700 MPa compression. The increase of fractal dimension of shale formation rocks after compression indicates that the pore structure gets rougher and more heterogeneous. It reveals that the pore structure and pore-system of shale rock experience a very complexed evolution during the compression, including compressing, cementing, splitting and vanishing. This work provides some guidelines for the rational design of stimulation technologies to improve shale oil and gas recovery, and the carbon sequestration in deep earth formations.

1. Introduction

In recent years, with the breakthrough of hydraulic fracturing and in-situ conversion technologies [1,2], the successful exploitation of hydrocarbons from shale reservoirs has become the most important growth point of global oil and gas [3,4]. Currently the hydrocarbon content per unit volume of shale produced to the ground is estimated to be only about 5–15% [1], which remains a big challenge to the urgent demand for the enhanced oil and gas recovery. Various methods such as advancing CO_2 enhanced oil recovery, artificial heating, etc. have been developed to improve the oil and gas production [5–7]. The difficulty of shale oil and gas extraction comes from its occurrence characteristics, such as deep stratum (usually below 3 km), complex crustal stress, extremely low permeability (10^{-9}–10^{-7} darcy), and low porosity (2–10%), etc. [8–11] Most of shale oil or gas occurs in the pore structure of kerogen (organic matter) with diameter of 0.5 nm–100 nm in the form of adsorption [12–15], which makes it one of the most important topics to improve hydrocarbon production.

Despite the critical importance of shale pore system as the space and channel for hydrocarbon generation, adsorption, migration and storage of shale oil and gas, its evolution with the action of stress remains unexplored. It is generally believed that the pore system of source rocks is formed and evolves gradually in the long geological history under the action of in-situ stress and geothermal energy, and is linked to maturity of kerogen [16]. In addition to geological evolution, artificial stimulation technologies such as hydraulic fracturing or in-situ conversion can also greatly change the pore structure in the kerogen or shale [17–20]. Hydraulic fracturing, or fracturing of hydrocarbon bearing rocks is an established technology for the development of shale oil and gas [21]. Fig. 1 shows a multiscale view of fracturing process. Powerful pumps on the fracturing truck or dill platform inject the high-energy pressurized fracturing fluid into tight shale formations. The fluid, whether water base (99% water and other additives) or waterless (also known as "CO_2 fracturing"), usually was consumed volume of $(1\sim8) \times 10^4$ m^3 for a single well [22,23]. Such a huge amount of fluid fractures the formation rocks in favor of even advancing of injected fluid. At the same time, the proppants contained in the fluid is transported to the crack tips and settled down after the fluid flowback (~15%), keeping the rock cracks open [24]. It is naturally that in the process of pumping fluid into the formation to promote the initiation, propagation and long-term opening of rock cracks, the mechanical behavior of the shale stratum is

* Corresponding author. State Key Laboratory of Nonlinear Mechanics, Institute of Mechanics, Chinese Academy of Sciences, Beijing, 100190, China.
E-mail address: yzhao@imech.ac.cn (Y.-P. Zhao).

https://doi.org/10.1016/j.energy.2023.127913
Received 20 March 2022; Received in revised form 19 May 2023; Accepted 21 May 2023
Available online 24 May 2023
0360-5442/

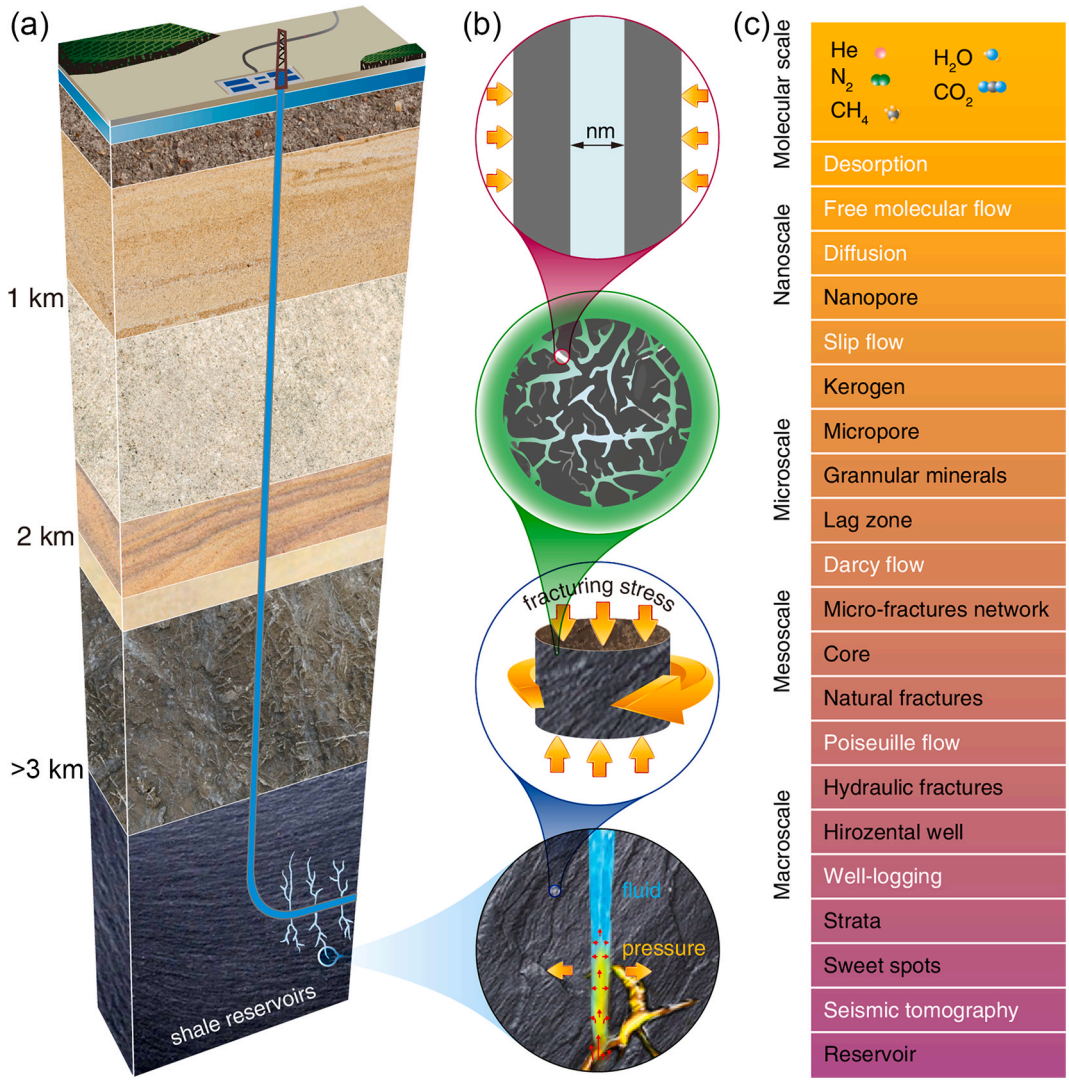

Fig. 1. Multiscale view of hydrocarbon recovery from shale formations. (a) Hydraulic fracturing. (b) Coupling effects of fracturing stress and crustal stress on the pore structure and adsorption-desorption. (c) Topics from nanoscale to macroscale.

directly dominated by the hydraulic pressure and the crustal stress. With the further injection of fracturing fluid, the rocks on both sides of the crack are compressed and deformed. As shown in Fig. 1(b), when the nanoporous shale subjects to a changing stress field (primarily compressive), its pore system evolves, resulting an inseparable varying in adsorption-desorption of oil and gas. On larger scales, the flow of oil and gas from molecular to continuum, well-logging and even seismic tomograph may also make a big difference, as illustrated in Fig. 1(c). Similarly, in the process of CO_2 storage (carbon sequestration), the injected gas and the pressure generated will compress the rock reservoir, thereby causing the pore system to evolve. In this respect, it is quite important to reveal the evolution mechanism of pore structure of shale formation rocks, which may affect the recovery to a great extent.

Liang et al. [25] studied the evolution of pore structure in gas shale from the detachment deformation belt by mercury injection capillary pressure and low-pressure gas adsorption, and found that the structural deformation affected the evolution of pore size distribution. Ibanez and Kronenberg [26] investigated the mechanical properties and deformation mechanism of shale from micro-structural indicators in triaxial compression experiments. Pan et al. [27] revealed that coalbed methane sorption is related to coal deformation structures at different pressures. Ismail and Zoback [28] found that the clay-rich shale has a higher pore throat compressibility and result in higher permeability reduction at increasing effective stress. Zhang et al. [29] revealed the relationship between the stress sensitivity and pore structure of shale. Several previous studies have been conducted to reveal the impact of stress or adsorption on the porosity and/or permeability of shale rocks [30–33], which also provide important reference to study the evolution of pore structures of shale. Generally, previous studies mainly focused on the relationships between the shale porosity and permeability and the effective stress, and the evaluation of micro-cracks and well performance in shale from stress sensitivity. All these studies show that, on the one hand, stress sensitivity is extremely important to the development of shale oil and gas. On the other hand, there are also some shortcomings in the current studies of stress sensitivity, such as it is still not clear that how the BET specific surface area, the pore size distribution, the pore volume, and the fractal dimension of shale rocks change with the compressive stress.

In this study, we carry out confined compression tests on oil shale formation rocks with varied terminal stresses. Then, low temperature nitrogen adsorption measurements and scanning electron microscopy are employed to analyze the adsorption-desorption process and pore structure evolution, including BET specific surface area, pore size distribution, total pore volume and fractal dimension.

2. Materials and methods

2.1. Preparation of shale samples

The shale formation rock used in this study is from shale oil fields of the Songliao Basin (Northeast China), which is characterized by high

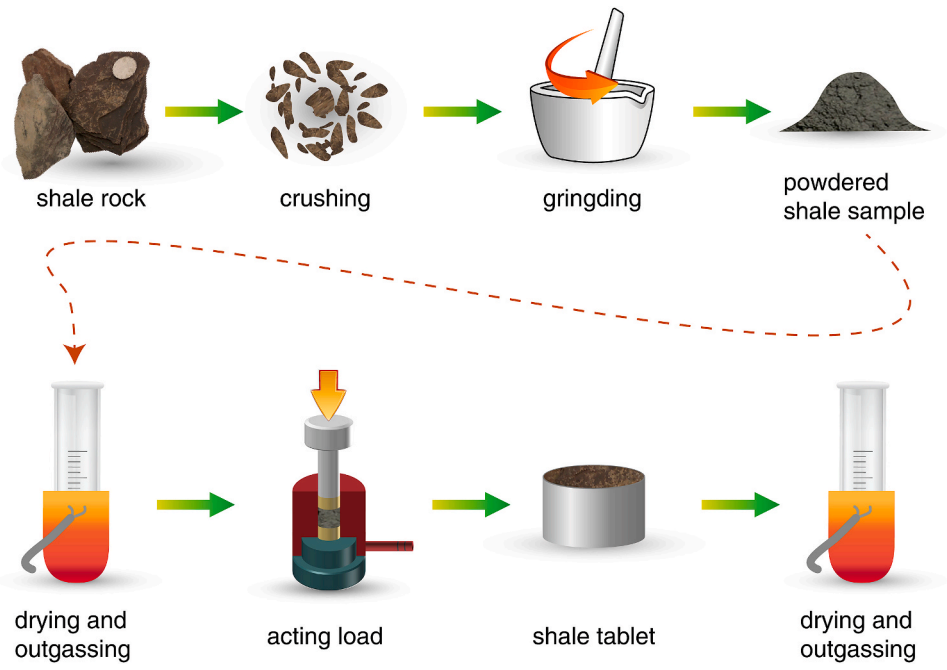

Fig. 2. Experimental preparation process for shale samples.

organic matter content and rich minerals [34]. Considering that the large modulus of shale and the small diameter (~10 mm) of the sample tube of the physical adsorption apparatus (standard instrument), firstly we crushed the rock into particles because of the sample requirements for testing the adsorption-desorption isotherms. After that the shale particles were compressed by a tablet press machine. Due to the underground stress field is quite complex, and in many cases the tectonic stress will involve large pressures, the applied stresses were set in the range of 50 MPa–700 MPa. The purpose of applying stresses is to study the corresponding changes of the pore structure of shale particles. Finally, the evolution of adsorption-desorption and pore structure of shale samples was tested. The sample preparation steps are shown in Fig. 2 and as follows.

(1) Crushing. Use geological hammer to break the whole shale rock into small particles with a diameter of several millimeters. The hammered particles or shale were not select for the experiment. Therefore, the shale particles used in the later experiments did not undergo compression during the crushing process. The crushing process is the common process before the low-temperature nitrogen test [35,36]. The hammered particles or shale were not select for the experiment. Therefore, the shale particles used in the later experiments did not undergo compression during the crushing process.
(2) Grinding. Grind the crushed particles by an agate mortar, and then screened by a 50-target standard sieve to obtain particles with 50~100 mesh. The selection of the particular particle size was based on our preliminary experiments, which showed that the optimal particle size for the low-temperature nitrogen adsorption test is about 0.1 mm~0.3 mm (50~100 mesh).
(3) Drying and outgassing. Put the ground shale particles into sample tube (be careful not to contaminate the tube mouth) and seal the tube with a one-way plug. Install the tube to the degassing station of an adsorption instrument to outgas the sample. The set temperature and time are listed in Table 1.

Table 1
The parameters of shale sample in the drying and outgassing experiments.

Evacution Phase		Heating Phase	
Temperature ramp rate	10.0 °C/min	Ramp rate	10.0 °C/min
Target temperature	65 °C	Hold temperature	65 °C
Evacution rate	5.0 mmHg/s	Hold time	240 min
Unrestricted evac. From	5.0 mmHg	–	–
Vacuum level	500 μmHg	Evacuation and Heating Phase	
Evacuation time	30 min	Hold pressure	100 mmHg

(4) Compressing. Take 0.5 g sample and put into a cylindrical steel mold each time. Compress it with a triaxial apparatus (Jingtuo, PC-12) with stress of 50 MPa, 100 MPa, 200 MPa, 300 MPa, 400 MPa, 500 MPa, 600 MPa and 700 MPa. The compressed samples were labeled as #2~#9, and the uncompressed sample was #1. Subsequently, use a vernier caliper to measure the length of compression, so as to calculate the strain of the samples under different loads. We have weighed at least 5 groups of each shale sample #1~#9 and placed them into the same mold, respectively, with an initial height error <0.5%. Since the shale is rich in organic matters, clays (mainly illite and chlorite), carbonates (calcite and dolomite), etc., the shale particles were cemented together to form core-like samples under triaxial compressions.
(5) Drying and outgassing. Dry and outgas the above nine shale samples once more as Step (3).

2.2. Low temperature nitrogen adsorption test

In this work, we adopt the low-temperature nitrogen adsorption to study the evolution of pore structure of compressed shale samples. The low temperature nitrogen adsorption test is a standard method recommended by International Union of Pure and Applied Chemistry (IUPAC), which used adsorption-desorption isotherms to reveal the quantitative BET specific surface area, the pore size distribution and pore volume. It

uses nitrogen as the adsorbent molecule to adsorb on the surface and pores of adsorbent, and measures the adsorption amount according to the relationship between volume and pressure before and after gas adsorption (i.e., volumetric method) [37]. The specific surface area, pore size distribution, pore volume and fractal dimension of the samples can be evaluated according to the adsorption isotherms combined with specific models.

The physical adsorption apparatus (ASAP 2020 Plus, Micromeritics) was used to conduct the low-temperature nitrogen adsorption experiment, which includes a molecular pump, low-pressure sensors and other systems, as shown in Fig. 3. The fluids used in the tests were high-purity nitrogen and high-purity helium (both purity >99.999%), liquid nitrogen (77 K), etc. Nitrogen has a series of advantages in the test, such as chemical inactivity, difficult to react with other substances at low/normal temperature, safety, non-toxicity and easy to obtain [33]. Most importantly, its molecular diameter is 0.37 nm, making it an ideal molecular probe to study micropores mesopores of porous media. According to our previous studies [12,33], pores in shale are mainly mesopores (2–50 nm). Therefore, we adopted the mesopores method to measure the specific surface area and pore size distribution of the nine shale samples obtained in subsection 2.1. The core-like samples were break into pieces before the low temperature nitrogen adsorption-desorption experiments. The experimental preparation and procedure for the low temperature nitrogen adsorption test are listed as follows.

(1) Experimental preparation
   1) Washing: Wash and clean the sample test tube and filler rod with distilled water and ethanol, then dry them in an oven, and then cool them naturally;
   2) Degassing: Install the empty sample tube to the degassing station of the adsorption instrument, then perform degassing, and then backfill the gas;
   3) Weighing 1: Take the sample tube from the degassing station, use an analytical balance to weigh the mass of the sample test tube + one-way plug (accurate to 0.0001 g), and record it as M_1;
   4) Sample setting: Put the shale sample prepared in subsection 2.1 into the sample test tube, and plug the tube mouth with a one-way plug;
   5) Weighing 2: Weigh the mass of the sample test tube + one-way plug + sample, record it as M_2;
   6) Degassing: Install the sample test tube to the degassing station of the adsorption instrument, put on a heating mantle, and then degas and backfill the shale sample with gas. The degassing parameters are consistent with Table 1;
   7) Weighing 3: Remove the sample test tube from the degassing station, and weigh the total mass of the degassed sample test tube + one-way plug + and sample again, record it as M_3;
   8) Inserting the filler rod: Remove the one-way plug, insert the filler rod, and then seal the sample test tube with the one-way plug. The filler rod can reduce only space volume of the test tube, thereby improving the test accuracy of low specific surface adsorbents;
   9) Sleeve: Place the sample test tube in the heating mantle.

(2) Experimental procedure
   1) Transfer the sample test tube to the analytical station of the adsorption instrument, install the connector and the sealing ring at the head of the tube and tighten it;
   2) Fit the white foam cap of the mouth of Dewar bottle onto the sample tube, screw on the p_0 tube and move it right behind the sample test tube;
   3) Use a liquid nitrogen gun to fill the Dewar bottle with liquid nitrogen, and place it on the lifting platform under the sample test tube;
   4) Analyze the sample and generate analysis reports.

2.3. SEM observation

The purpose of the SEM is to observe and verify the change of the microstructure of the shale samples after applied compressed stress. The microstructure of the 9 shale samples obtained in subsection 2.1 were observed by the SEM (FESEM, G300; Carl Zeiss, Germany). The shale samples for the SEM observation were adhered to a dual adhesive tape, which was adhered to SEM sample stage. Because the shale rock is non-conductive, the samples have been sprayed with platinum for 300 s before being placed into the SEM scanning cavity.

3. Results and discussions

3.1. Stress-strain relation

In this study the “stress-strain” are not the true stress and strain of shale rock, but a compaction process of shale particles, in which there are a large number of voids. As the compressive stress increased, the shale particles were cemented, deformed and even fractured. The shale rock particles were compressed in the mold using a triaxial apparatus with a set stress marked as σ_i. After that the stress was removed, and a

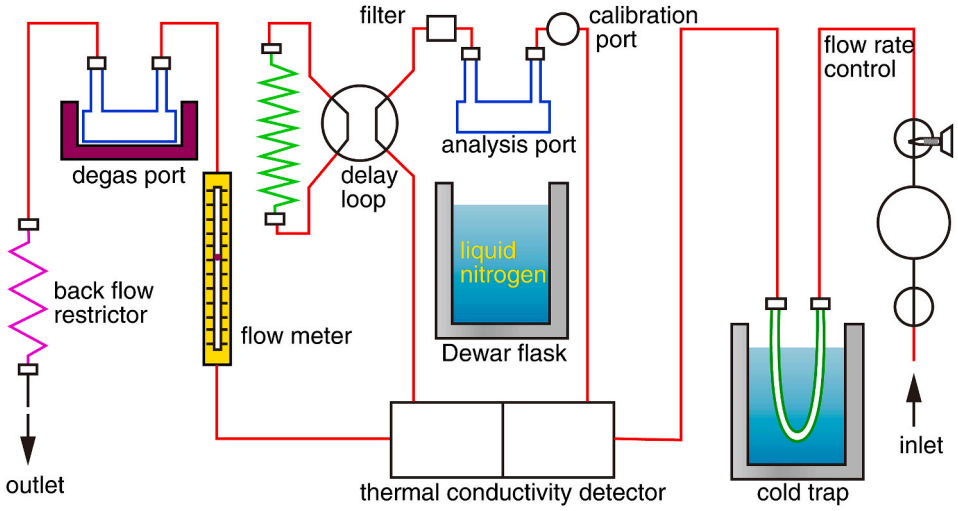

Fig. 3. The low temperature nitrogen adsorption experiments (Modified from Ref. [38]).

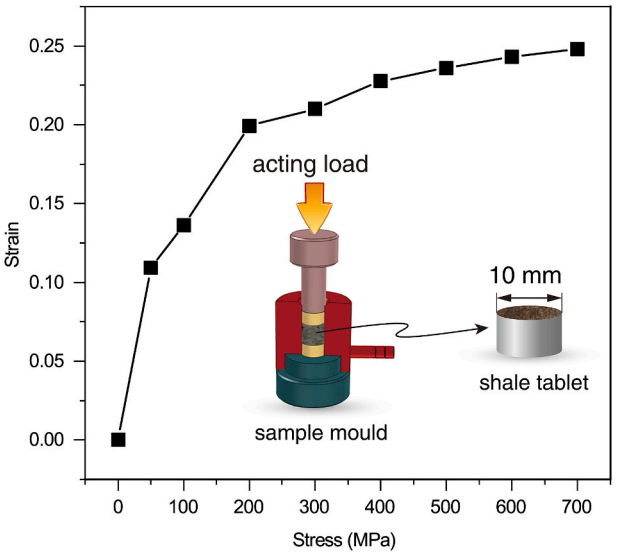

Fig. 4. The stress-strain diagram of the shale samples. The diameter of the shale samples was 10 mm. The pressures settled in the experiments were 50 MPa, 100 MPa, 200 MPa, 300 MPa, 400 MPa, 500 MPa, 600 MPa, and 700 MPa, respectively.

vernier caliper was employed to measure the height of compression, which was used to calculate the strain ε_i of the samples after applied σ_i. Accordingly, we obtain a data set of (σ_i, ε_i) with the applied compression stress in the range of 50 MPa–700 MPa. Fig. 4 shows the stress-strain diagram of shale samples under different effective stress. In fact, the "strain" ε_i here is not the true strain of shale rock, but a compaction process of shale particles, in which there are a large number of voids. The compression of shale samples by the triaxial apparatus is a continuous compaction process. As the compressive stress increased, the loose shale particles were compacted, deformed, even fractured cemented. It can be seen that in the early stage of the compression (0–200 MPa), the strain of the shale sample increased sharply, which was the process of shale particles from loose to compact. The main deformation of the shale samples was the sharp decrease of the pores between the particles. In the middle and late stages (200–700 MPa), the deformation became less steep at the same load gradient, mainly because the gap between particles has almost disappeared after the early compressive. The deformation of samples at late stages was primary the extrusion between shale particles.

3.2. Adsorption-desorption isotherms

The adsorption-desorption isotherms of the shale samples subjected to different compressive stresses are shown in Fig. 5. It can be seen that the adsorption type of shale is physisorption, which is different from the chemisorption or mechanisorption [39,40]. According to the classification of adsorption-desorption isotherms given by the International Union of Pure and Applied Chemistry (IUPAC), the isotherms of shale samples are close to the type IV, indicating that there are a large number of mesopores in the samples [41]. The adsorption process can be divided into the following three stages based on the change of adsorption capacity versus relative pressure.

(1) The low-pressure adsorption stage ($0< p/p_0 \leq 0.42$). The adsorption capacity increases slowly when the relative pressure increases, and the isotherm shows slow ascending, which corresponds to the monolayer adsorption of nitrogen molecules on the surface and pores of shale samples.
(2) The transition adsorption stage ($0.42< p/p_0 \leq 0.9$). With the increase of relative pressure, the adsorption capacity increases fast, resulting in the rapid rise of isotherm. It corresponds to the multilayer adsorption of nitrogen molecules on the sample, and the capillary condensation [40] occurs in the pores after the relative pressure exceeded about 0.42.
(3) The high-pressure adsorption stage ($p/p_0 > 0.9$). The adsorption capacity of the sample increases rapidly when increasing the relative pressure, owing to the gas pressure is close to the saturated vapor pressure and there is no limited adsorption. In this stage, the adsorbate molecules undergo significant capillary condensation on the samples. The adsorption capacity becomes smaller as the stress increases, indicating that the volume of macropores decreases after compression.

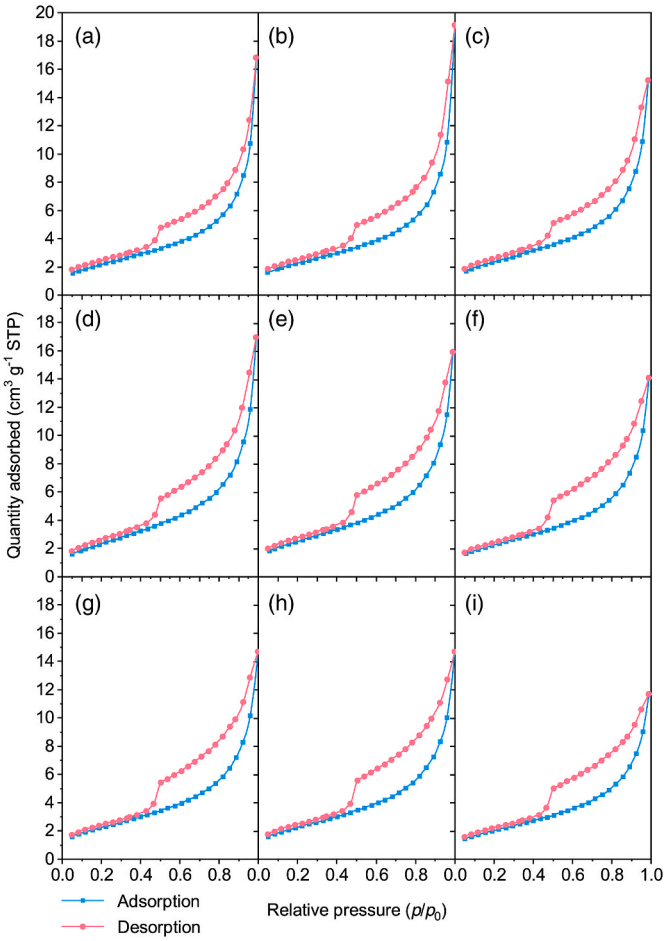

Fig. 5. The adsorption-desorption isotherms of shale samples after compression. (ai) represent #1∼#9 shale samples subject to different compressive stresses, respectively.

Similarly, the desorption branch can also be divided into three stages as following.

(1) The high-pressure desorption stage ($p/p_0 > 0.9$). The trend is the approximately inverse of the adsorption process. The desorption isotherm drops sharply versus the relative pressure, indicating the fast evaporation of the adsorbate condensate in the open macropores of the samples.
(2) The transition desorption stage ($0.42< p/p_0 \leq 0.9$). The desorption isotherm decreases fast when the relative pressure decreases due primarily to the evaporation in the meso- or macro-porous. The adsorption and desorption branches of isotherms do not coincident: the former is below the latter, resulting in an obvious hysteresis loop [42]. This is because the change of free energies of

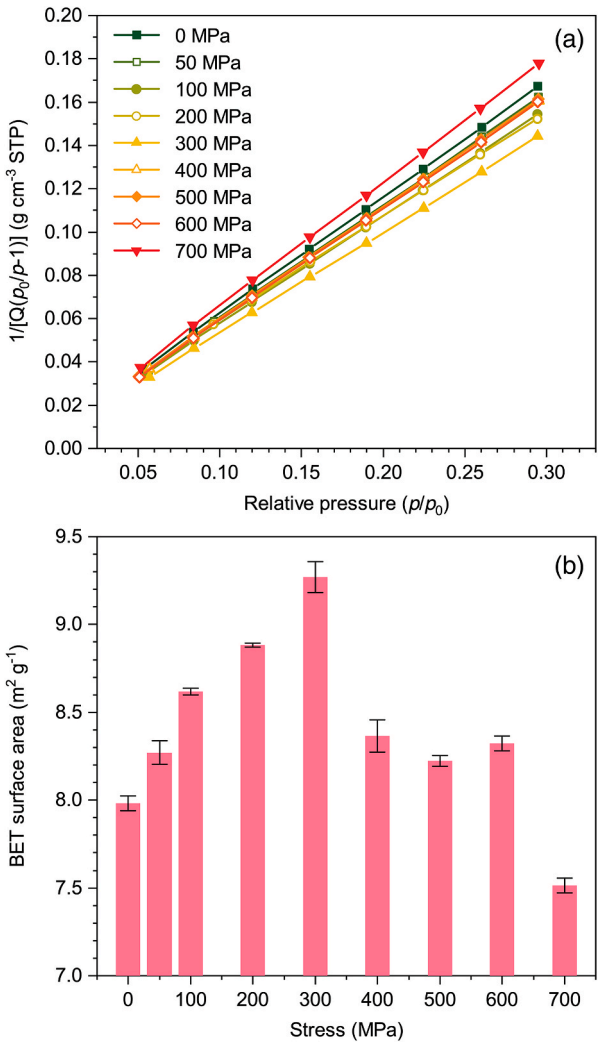

Fig. 6. (A) The BET plot and (b) The BET specific surface area of the nine shale samples compressed with different stresses.

capillary condensation and evaporation is different under the same pressure.

(3) The low-pressure desorption stage ($0< p/p_0 \leq 0.42$). The desorption branches show an obvious inflection point when the relative pressure is about 0.42, and then the trend is almost consistent with the adsorption one. It mainly represents the monolayer desorption or desorption in micropores.

It can be seen from Fig. 5 that the adsorbed capacity of N_2 decreases with the increasing compressive stresses, indicating that the applied load has a negative effect on adsorption, which is opposite to the surface stress induced by adsorption [43]. In the low-pressure adsorption-desorption stage, although the two branches almost coincide, the desorption one is slightly higher than the adsorption one. It is generally believed that this slight low-pressure hysteresis is related to the expansion of non-rigid porous structures or irreversible adsorption-desorption of pores. For example, when the adsorbent diffuses into the adsorbate matrix, or the adsorbate molecule is equivalent to the pore in diameter, it cannot escape in the desorption process, resulting in such hysteresis.

As for the obvious hysteresis when the relative pressure exceeds 0.42, it is caused by the capillary condensation of adsorbent molecules in the shale pores. The hysteresis loop of different types of pores are quite different. According to the classification of hysteresis loops by IUPAC, the loops in Fig. 5 are close to H3 type, indicating that the pore morphology of shale samples is mainly slit-shaped or parallel plate-shaped [41,44].

3.3. BET specific surface area

In order to obtain the specific surface area of the shale samples, the multi-point BET method [45] was employed to analyze the isotherms in Fig. 5. This method requires the value to be taken in adsorption branch with the relative pressure of 0.05–0.3. Fig. 6(a) shows the BET plot of the nine shale samples, all of which are linear.

Table 2 lists the adsorption capacity Q_m (cm^3/g) of the single molecular layer required to completely cover the sample surface, which were obtained according to the slope and intercept of curves in Fig. 6(a). It can be seen that Q_m first increases and then decreases as the compressive stress increases.

Based on Table 2, the specific surface area calculated by the BET theory is plot in Fig. 6(b). As shown in the figure, the BET specific surface area of the shale samples is between 7.5–9.3 m^2/g, and evolves consistently with the monolayer adsorption capacity Q_m, that is, it first increases and then decreases versus the compressive stress. In the first stage (0–300 MPa), the BET specific surface area increases with the increase of the compressive stress. While in the late stage (300–700 MPa), the BET specific surface area decreases as the stress increasing. At last, the BET specific surface area is ~6% smaller than that of the uncompressed shale sample, and ~20% smaller than the peak BET specific surface area. According to Zhan et al. concluded in their recently work [36] that the BET specific surface area of shale is almost unaffected by the particles' size. Therefore, the prepared samples can be considered to represent the behavior of actual case in most cases.

3.4. Pore size distribution and pore volume

As shown in Fig. 7, the classic Barrett-Joyner-Halenda (BJH) theory was employed to evaluate the pore size distribution and the pore volume based on the adsorption-desorption isotherms of the shale samples [46]. Fig. 7 (a) is an enlarged view of pore size distribution that below 1.5 nm (micropores). It can be seen that after the compression, the pore size of micropores in the shale samples first increases to a certain extent, and then decreases gradually until it almost disappears.

As shown in Fig. 7 (b), the pore size distribution of the nine shale samples is bimodal. The pores are mainly mesoporous, and also contain a small amount of micropores. The peak position of all the samples did not change significantly. It should be noted that the peak value directly corresponds to the pore volume, and the peak width represents the dispersion and concentration of the pore size distribution. The first dominant peak of the nine shale samples is about 1.2 nm, indicating that the micropores contribute a little to the total pore volume. The second dominant peak value is about 2.0 nm, i.e., the critical point of micropore and mesoporous. The pore volume at this peak value is the largest, which the crest characteristics are obvious. There is no dominant peak when the pore size is greater than 2.0 nm. And the distribution curve decreases slowly, indicating that the overall distribution of mesoporous is relatively uniform, and gradually decreases versus the pore size. For

Table 2
The adsorption capacity of the single monolayer on the shale samples.

Sample	#1	#2	#3	#4	#5	#6	#7	#8	#9
Q_m (cm^3/g)	1.664	1.743	1.784	1.827	1.940	1.749	1.727	1.745	1.571

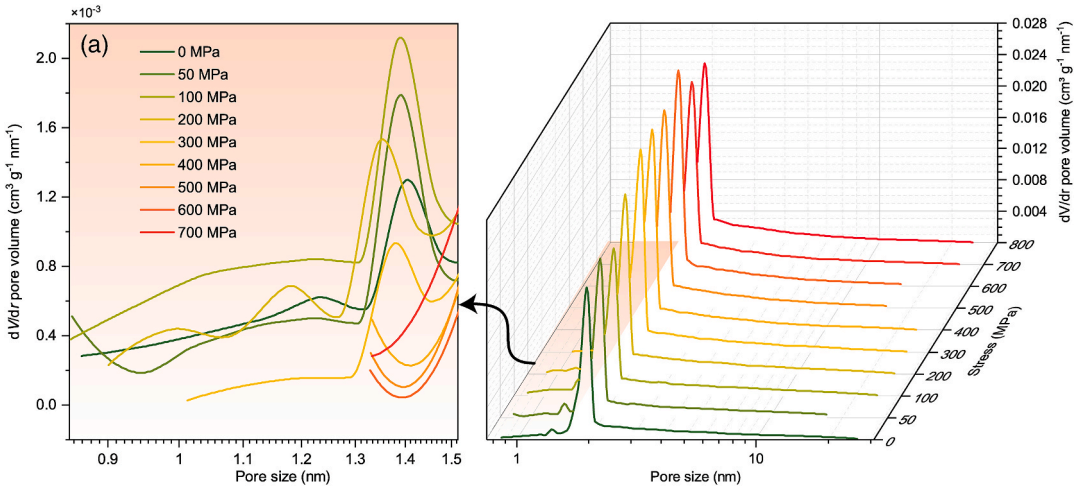

Fig. 7. The pore size distribution of the shale samples subjetcted to compressive stresses.

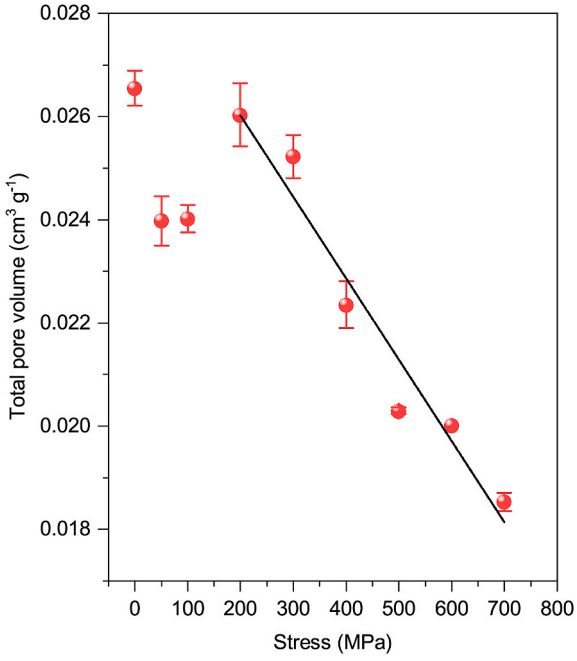

Fig. 8. The total pore volume of the nine shale samples versus compressive stress.

Table 3
The pore structure parameters of the shale samples.

Sample	Specific surface area (m^2/g)	Total pore volume (cm^3/g)	Average pore size (nm)
#1	7.9823	0.02655	5.13
#2	8.27105	0.02398	4.42
#3	8.61815	0.02402	4.29
#4	8.88235	0.02603	4.27
#5	9.2702	0.02522	4.06
#6	8.36415	0.02235	3.74
#7	8.22333	0.02029	3.40
#8	8.32305	0.02002	3.30
#9	7.5143	0.01853	3.38

the shale samples subjected to increasing compressive stresses, the peak value of the second dominant peaks decreases slightly at first and then increases again, indicating that the pore size distribution around the peaks has changed.

Fig. 8 shows the total pore volume versus compressive stress by integral calculation of pore size distribution of Fig. 7(b), which reveals that the total pore volume of the shale samples is greatly affected by the compression. With the increase of the compressive stress, the total pore volume mainly undergoes three stages of decrease, increase and decrease. Under the stress of 0–100 MPa, it decreases by ~10%, and then almost increases to the initial state at 200 MPa. Thenceforth, the total pore volume decreases approximately linearly. At 700 MPa, it decreases by ~30% compared with the initial state. We propose a concept of "residual pore volume (RPV)" to describe the remaining pore volume of samples after compression. RPV is the actual pore volume of shale formations rocks in fracturing production, which is very important for desorption, displacement and migration of shale oil and gas.

Table 3 lists the BET specific surface area, total pore volume and average pore size of the nine shale samples. It can be seen that the BET specific surface area and the total pore volume show opposite trends in the initial stage (0–300 MPa), while are consistent in the middle and late stage, i.e., both decrease with the increase of compressive stress. In addition, the average pore size decreases when the applied stress increases.

Recently both Han and co-workers [47], Zhan and co-workers [36] both revealed that particle size has a considerable effect on pore volume and pore size distribution measurement, with 120–160 mesh size samples may the optimum for the study of pore volume and pore size distribution using low temperature nitrogen adsorption test. Since our shale sample (from Songliao Basin) is different from theirs (from Southern Sichuan), based on our preliminary experiments, we selected the optimal particle size to be 50–100 mesh. The sample selection and preparation methods were similar to their study and can be considered representative of actual case behavior.

3.5. *Fractal dimension of shale samples*

The fractal dimension reflects the effectiveness of space occupied by complex objects, and is a measure of the irregularity. For shale formation rocks, the fractal dimension interprets the comprehensive pore structure parameters including surface roughness, volume and pore size [48], that is, revealing the complexity and heterogeneity of pore structure quantitatively. Generally, the fractal dimension is measured based on the low-temperature nitrogen adsorption isotherms combined with the Frenkel-Halsey-Hill (FHH) theory [49,50], which describes the multilayer adsorption on solid surface as follows:

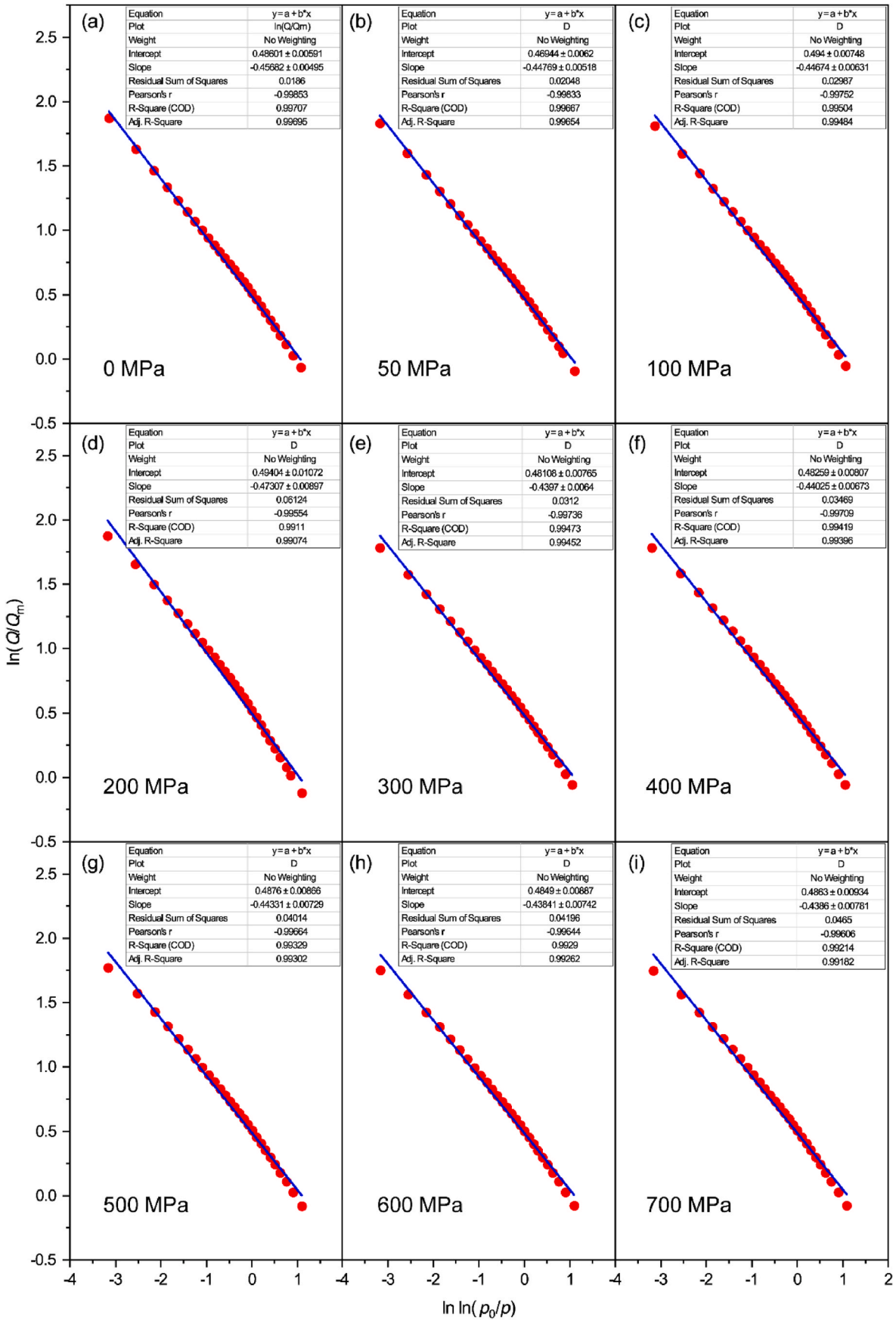

Fig. 9. The linear fitting curves of ln ln (p_0/p) versus ln (Q/Q_m) for calculating the fractal dimensions of shale samples after applied different compressive stresses.

Table 4
The fractal dimension of shale samples subjected to compressive stresses.

Sample	#1	#2	#3	#4	#5	#6	#7	#8	#9
D	2.543	2.552	2.553	2.527	2.560	2.560	2.557	2.562	2.561

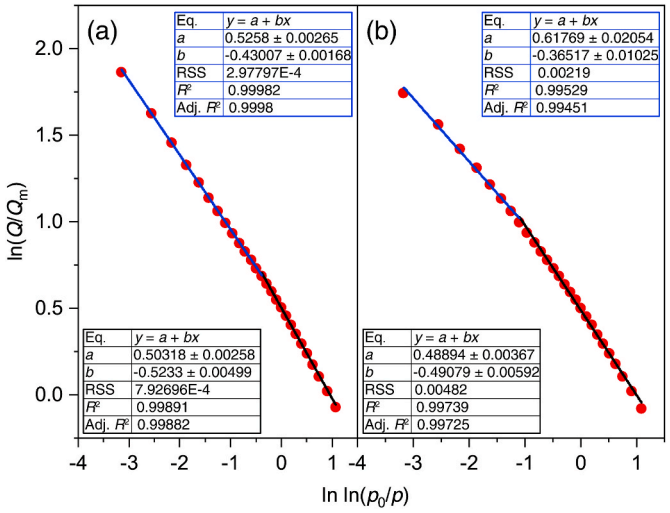

Fig. 10. Segmental calculation of the fractal dimension of shale samples. (a) Uncompressed; (b) 700 MPa.

$$Q/Q_m \approx \left[RT\ln\left(p_0/p\right)\right]^{-\frac{1}{s}} \tag{1}$$

where Q is the adsorption volume; s is a parameter describing the shape of an isotherm ($s = 2.5$–2.7).

Pfeifer et al. further developed the application of FHH theory in calculating the fractal dimension D of porous materials [50–52]:

$$\ln\left(Q/Q_m\right) = \text{constant} + \frac{D-3}{3}\left[\ln\ln\left(p_0/p\right)\right] \tag{2}$$

$$\ln\left(Q/Q_m\right) = \text{constant} + (D-3)\left[\ln\ln\left(p_0/p\right)\right] \tag{3}$$

Eqs. (2) and (3) applies to the adsorption process dominated by the van der Waals interaction and the solid-liquid interface tension, respectively. In this study, Eq. (3) is suitable for calculating the fractal dimension of shale samples. In combination with Eq. (3) and the adsorption-desorption isotherms of the nine shale samples, we plotted the linear fitting curves of $\ln\ln(p_0/p)$ versus $\ln(Q/Q_m)$ used to calculate the fractal dimensions of the nine shale samples after applied different compressive stresses, as shown in Fig. 9. It can be seen that the linear regression coefficient of the experimental results is very high ($R^2 >$ 0.99), indicating that the pore structure of the shale samples has obvious fractal characteristics. Therefore, the fractal dimension of each shale sample can be calculated by combined Fig. 9 and Eq. (3), as listed in Table 4. It can be seen that the fractal dimension of the nine shale samples ranged from 2.527 to 2.562, indicating that the compressive stress improves some aspects of fractal dimension, but it is a small boost. It should be noted that as the closer the fractal dimension approaches to 2, the pore surface becomes more regular (smooth). Otherwise, it becomes more irregular (rough) when the fractal dimension approaches to 3, i.e., that is, the pore structure is more complex and the pore connectivity is worse, and the heterogeneity is stronger.

Although the coefficient of determination R^2 exceeds 0.99, it can be further divided into two segments for linear fitting. Firstly, we roughly divide the data points into two parts based on Fig. 9, and then perform linear fitting on them. The intersection point of the two fitted lines is the interval of the segmentation, as shown in Fig. 10. The shale samples without compression and applied 700 MPa stress were taken as examples, the data points were divided into two parts for the linear fitting. Therefore, four fractal dimensions of the two samples were calculated as listed in Table 5, where D_1 and D_2 respectively correspond to the medium- and low-pressure adsorption sections. They were calculated from the slopes of the blue and black fitting lines in Fig. 10. It can be seen that the fractal dimension of macropores in both samples is larger than that of mesoporous pores ($D_1 > D_2$), indicating rougher and more heterogeneous pore structures. After applied compressive stress, the fractal dimension of the shale samples increases, indicating that the pore surfaces become more complex. The irregularity of pore shape is higher, and the connectivity becomes worser.

Table 5
Segmental fractal dimensions of shale samples.

Sample	#1	#9
D_1	2.570	2.635
D_2	2.477	2.509

3.6. Microstructure change

Fig. 11 shows the SEM micrograph of the shale samples. As the compressive stress increased, the shale particles experiences processes of loose → compact → deformed → fractured → cemented. Fig. 11(a) is the uncompressed shale sample, which has small particles and is relatively loose. Fig. 11(b and c) are the enlarged view of (a), showing that the shale minerals have schistose appearance. It originated during the formation of shale, when the minerals were oriented under sedimentation and compaction to form bedding layers. Sub-micron slits or cracks and pores of 10–100 nm can be seen between the layers, which are very important for the adsorption and diffusion of oil and gas [53].

Fig. 11(d–i) show the SEM images of the shale samples after compressed. As the applied stress increases, the shale particles become closer, and the boundary between the particles becomes almost indistinguishable. At the same time, the profile surfaces get rougher and more irregular, which verifies the results of fractal dimension. As shown in Fig. 11(g–i), two types of microcracks occurred in the compressed shale sample: serrated and straight, both of which are hundreds of nanometers in width. These two types of microcracks were produced in different minerals caused by different forms of compression failure. In the shale formation rocks, quartz, feldspar etc. Minerals have high strength, usually form straight cracks. While the strength of carbonate and clay minerals is relatively small, resulting in more complex cracks such as serrated. The fracture of shale particles can also explain why at some stage the BET specific surface area and the pore volume increase with the increase of external stress, and then decrease when the particles were cemented.

4. Conclusions

In this paper, we studied the pore structure evolution of shales subjected to different compressive stresses using nitrogen adsorption measurements and SEM. The experimental results show that BET surface area, pore volume and fractal dimension of shale all changed with the compressive stress. The BET specific surface area of shale samples increases with the increase of applied stress when it less than 300 MPa. When the applied stress exceeds 300 MPa, the BET specific surface area

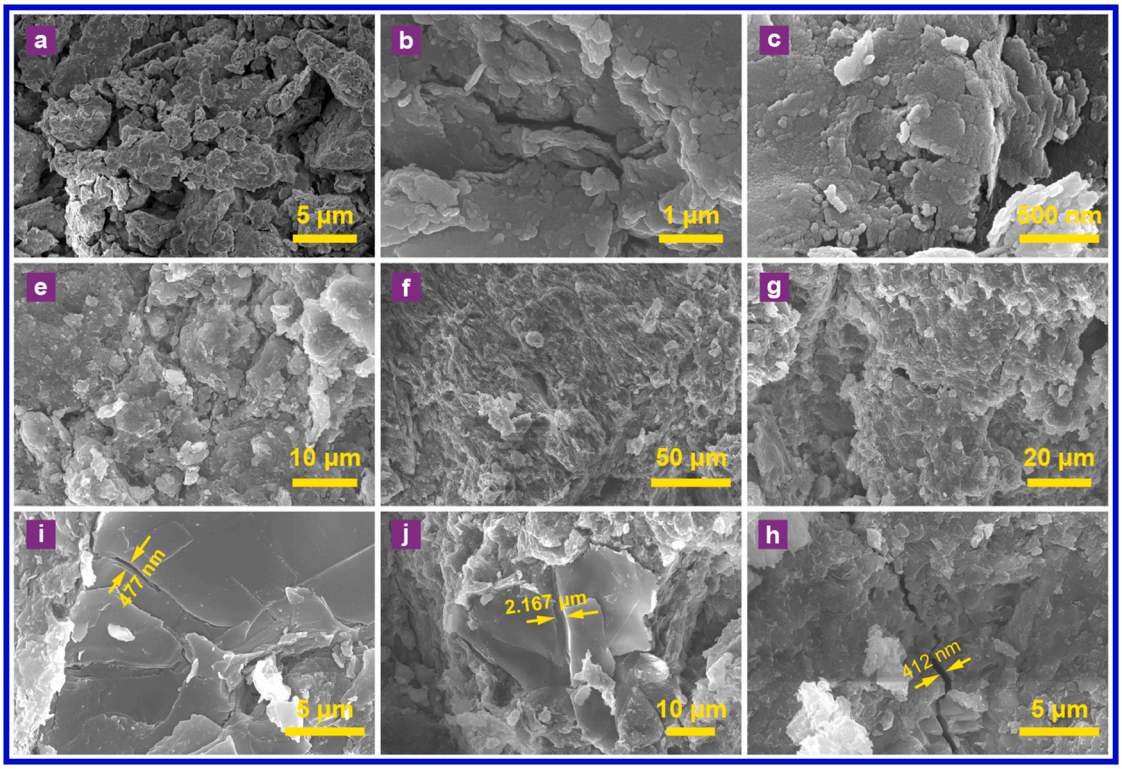

Fig. 11. The SEM micrographs of the shale samples.

decreases. In the process of shale compression, the pore volume goes through the stages of decreasing, increasing and continuously decreasing. The fractal dimension of the compressed shale rock is higher than that of the uncompressed shale rock, which indicates that the pore structure becomes more irregular under compressive stress. This work may provide some guidance for ultra-deep underground engineering.

Credit author statement

Xianfu Huang: Investigation, Methodology, Formal analysis, Visualization, Writing. **Ya-Pu Zhao**: Supervision, Project administration.

Declaration of competing interest

The authors declare that they have no known competing financial interests or personal relationships that could have appeared to influence the work reported in this paper.

Data availability

Data will be made available on request.

Acknowledgement

This work was jointly supported by the PetroChina Innovation Foundation (2019D-5007-0102), the National Natural Science Foundation of China (NSFC, Grant No. 12032019, 12241205, 11702299), and National Key R&D Program of China (2022YFA1200061).

References

[1] Bažant ZP, Salviato M, Chau VT, Viswanathan H, Zubelewicz A. Why fracking works. J Appl Mech-T ASME 2014;81:101010.
[2] Kang Z, Zhao Y, Yang D. Review of oil shale in-situ conversion technology. Appl Energy 2020;269:115121.
[3] Peplow M. The great gas gold rush. Nature 2017;550:26–8.
[4] Hughes JD. A reality check on the shale revolution. Nature 2013;494:307–8.
[5] Phong N, Carey JW, Viswanathan HS, Porter M. Effectiveness of supercritical-CO_2 and N_2 huff-and-puff methods of enhanced oil recovery in shale fracture networks using microfluidic experiments. Appl Energy 2018;230:160–74.
[6] Lin K, Zhao Y-P. Entropy and enthalpy changes during adsorption and displacement of shale gas. Energy 2021;221:119854.
[7] Chen B, Pawar RJ. Characterization of CO_2 storage and enhanced oil recovery in residual oil zones. Energy 2019;183:291–304.
[8] Liu K, Ostadhassan M, Gentzis T, Fowler H. Image analysis of the pore structures: an intensive study for Middle Bakken. J Nat Gas Sci Eng 2019;61:32–45.
[9] Lee T, Bocquet L, Coasne B. Activated desorption at heterogeneous interfaces and long-time kinetics of hydrocarbon recovery from nanoporous media. Nat Commun 2016;7:11890.
[10] Kerr RA. Engineering Fracture MechanicsNatural gas from shale bursts onto the scene. Science 2010;328:1624–6.
[11] Cueto-Felgueroso L, Juanes R. Forecasting long-term gas production from shale. Proc Natl Acad Sci USA 2013;110:19660–1.
[12] Huang X, Zhao Y-P. Characterization of pore structure, gas adsorption, and spontaneous imbibition in shale gas reservoirs. J Petrol Sci Eng 2017;159:197–204.
[13] Wang X, Huang X, Lin K, Zhao Y-P. The constructions and pyrolysis of 3D kerogen macromolecular models: experiments and simulations. Glob Chall 2019;3:1900006.
[14] Clarkson CR, Solano N, Bustin RM, Bustin AMM, Chalmers GRL, He L, et al. Pore structure characterization of North American shale gas reservoirs using USANS/SANS, gas adsorption, and mercury intrusion. Fuel 2013;103:606–16.
[15] Thomas JJ, Valenza JJ, Craddock PR, Bake KD, Pomerantz AE. The neutron scattering length density of kerogen and coal as determined by CH_3OH/CD_3OH exchange. Fuel 2014;117:801–8.
[16] Curtis ME, Cardott BJ, Sondergeld CH, Rai CS. Development of organic porosity in the Woodford Shale with increasing thermal maturity. Int J Coal Geol 2012;103:26–31.
[17] Daigle H, Hayman NW, Jiang H, Tian X, Jiang C. Multiscale pore networks and their effect on deformation and transport property alteration associated with hydraulic fracturing. Energy Proc 2017;125:71–9.
[18] Wang X, Zhao Y-P. The time-temperature-maturity relationship: a chemical kinetic model of kerogen evolution based on a developed molecule-maturity index. Fuel 2020;278:118264.
[19] Zhang Y, Yu B, Pan Z, Hou C, Zuo Q, Sun M. Effect of thermal maturity on shale pore structure: a combined study using extracted organic matter and bulk shale from Sichuan Basin, China. J Nat Gas Sci Eng 2020;74:103089.
[20] Hu Y, Liu G, Luo N, Gao F, Yue F, Gao T. Multi-field coupling deformation of rock and multi-scale flow of gas in shale gas extraction. Energy 2022;238:121666.
[21] Shen W, Yang F, Zhao Y-P. Unstable crack growth in hydraulic fracturing: the combined effects of pressure and shear stress for a power-law fluid. Eng Fract Mech 2020;225:106245.
[22] Clark CE, Horner RM, Harto CB. Life cycle water consumption for shale gas and conventional natural gas. Environ Sci Technol 2013;47:11829–36.

[23] Nicot J-P, Scanlon BR. Water use for shale-gas production in Texas, U.S. Environ Sci Technol 2012;46:3580–6.
[24] Katende A, O'Connell L, Rich A, Rutqvist J, Radonjic M. A comprehensive review of proppant embedment in shale reservoirs: experimentation, modeling and future prospects. J Nat Gas Sci Eng 2021;95:104143.
[25] Liang M, Wang Z, Gao L, Li C, Li H. Evolution of pore structure in gas shale related to structural deformation. Fuel 2017;197:310–9.
[26] Ibanez WD, Kronenberg AK. Experimental deformation of shale: mechanical properties and microstructural indicators of mechanisms. Int J Rock Mech Min Sci Geomech Abstr 1993;30:723–34.
[27] Pan J, Hou Q, Ju Y, Bai H, Zhao Y. Coalbed methane sorption related to coal deformation structures at different temperatures and pressures. Fuel 2012;102:760–5.
[28] Al Ismail MI, Zoback MD. Effects of rock mineralogy and pore structure on stress-dependent permeability of shale samples. Philos T R Soc A 2016;374:20150428.
[29] Zhang W, Wang Q, Ning Z, Zhang R, Huang L, Cheng Z. Relationship between the stress sensitivity and pore structure of shale. J Nat Gas Sci Eng 2018;59:440–51.
[30] Wu W, Zoback MD, Kohli AH. The impacts of effective stress and CO_2 sorption on the matrix permeability of shale reservoir rocks. Fuel 2017;203:179–86.
[31] Kamali-Asl A, Zoback MD, Kohli AH. Effects of supercritical CO2 on matrix permeability of unconventional formations. Energies 2021;14:1101.
[32] van Noort R, Yarushina V. Water, CO_2 and argon permeabilities of intact and fractured shale cores under stress. Rock Mech Rock Eng 2019;52:299–319.
[33] Huang X, Zhao Y-P, Wang X, Pan L. Adsorption-induced pore blocking and its mechanisms in nanoporous shale due to interactions with supercritical CO_2. J Petrol Sci Technol 2019;178:74–81.
[34] Hou L, Luo X, Han W, Lin S, Pang Z, Liu J. Geochemical evaluation of the hydrocarbon potential of shale oil and its correlation with different minerals–a case study of the TYP Shale in the Songliao Basin, China. Energy Fuel 2020;34:11998–2009.
[35] Smith JL, De Vries KL, Bushnell DJ, Brown WS. Fracture data and stress-strain behavior of rocks in triaxial compression. Exp Mech 1969;9:348–55.
[36] Zhan H, Li X, Hu Z, Duan X, Guo W, Li Y. Influence of particle size on the low-temperature nitrogen adsorption of deep shale in Southern Sichuan, China. Minerals 2022;12:302.
[37] Carrott P, Sing K. Multilayer adsorption of nitrogen and alkanes by non-porous carbons and silicas. Pure Appl Chem 1989;61:1835–40.
[38] Kenvin J. Characterization of powders and porous materials with pharmaceutical excipinent case studies. Retrieved from, https://www.micromeritics.com/Repository/Files/Pharma_Excipents_Kenvin_Presentation.pdf.
[39] Feng L, Qiu Y, Guo Q-H, Chen Z, Seale James SW, He K, et al. Active mechanisorption driven by pumping cassettes. Science 2021;374:1215–21.
[40] Zhao Y-P. Physical mechanics of surfaces and interfaces. Bejing: Science Press; 2012.
[41] Sing KS. Reporting physisorption data for gas/solid systems with special reference to the determination of surface area and porosity (Recommendations 1984). Pure Appl Chem 1985;57:603–19.
[42] Chen J, Wang F, Liu H, Wu H. Molecular mechanism of adsorption/desorption hysteresis:dynamics of shale gas in nanopores. Sci China Phys Mech Astron 2016;60:014611.
[43] Yang ZY, Wang ZQ, Zhao YP. Surface stress induced by adatoms adsorption on solid surfaces. Int J Nonlin Sci Num 2008;9:323–32.
[44] Chen C, Sun J, Zhang Y, Mu J, Li W, Song Y. Adsorption characteristics of CH_4 and CO_2 in organic-inorganic slitpores. Fuel 2020;265:116969.
[45] Brunauer S, Emmett PH, Teller E. Adsorption of gases in multimolecular layers. J Am Chem Soc 1938;60:309–19.
[46] Barrett EP, Joyner LG, Halenda PH. Computations from nitrogen isotherms. J Am Chem Soc 1951;73:373–80.
[47] Han H, Cao Y, Chen S-j, Lu J-g, Huang C-x, Zhu H-h. Influence of particle size on gas-adsorption experiments of shales: An example from a Longmaxi Shale sample from the Sichuan Basin, China. Fuel 2016;186:750–7.
[48] Lin K, Huang X, Zhao Y-P. Combining image recognition and simulation to reproduce the adsorption/desorption behaviors of shale gas. Energy Fuel 2020;34:258–69.
[49] Pierce C. The Frenkel-Halsey-Hill adsorption isotherm and capillary condensation. J Phys Chem 1960;64:1184–7.
[50] Pomonis PJ, Tsaousi ET. Frenkel-Halsey-Hill equation, dimensionality of adsorption, and pore anisotropy. Langmuir 2009;25:9986–94.
[51] Pfeifer P, Wu Y, Cole M, Krim J. Multilayer adsorptionon a fractally rough surface. Phys Rev Lett 1989;62:1997.
[52] Ismail IM, Pfeifer P. Fractal analysis and surface roughness of nonporous carbon fibers and carbon blacks. Langmuir 1994;10:1532–8.
[53] Chen C, Hu W, Sun J, Li W, Song Y. CH4 adsorption and diffusion in shale pores from molecular simulation and a model for CH4 adsorption in shale matrix. Int J Heat Mass Tran 2019;141:367–78.